

Deep Learning Enabled Time-Lapse 3D Cell Analysis

Jiaxiang Jiang^{**}, Amil Khan^{*}, S. Shailja^{*}, Samuel A. Belteton[†], Michael Goebel^{*}, Daniel B. Szymanski[†], and B.S. Manjunath^{**}

^{*} Department of Electrical and Computer Engineering, University of California,
Santa Barbara

[†] Department of Botany and Plant Pathology, Purdue University

Abstract

This paper presents a method for time-lapse 3D cell analysis. Specifically, we consider the problem of accurately localizing and quantitatively analyzing sub-cellular features, and for tracking individual cells from time-lapse 3D confocal cell image stacks. The heterogeneity of cells and the volume of multi-dimensional images presents a major challenge for fully automated analysis of morphogenesis and development of cells. This paper is motivated by the pavement cell growth process, and building a quantitative morphogenesis model. We propose a deep feature based segmentation method to accurately detect and label each cell region. An adjacency graph based method is used to extract sub-cellular features of the segmented cells. Finally, the robust graph based tracking algorithm using multiple cell features is proposed for associating cells at different time instances. Extensive experiment results are provided and demonstrate the robustness of the proposed method. The code is available on Github ¹ and the method is available as a service through the BisQue portal. ²

Index Terms

¹<https://github.com/UCSB-VRL/Time-lapse3DCellAnalysis>

²* corresponding authors

I. INTRODUCTION

The sizes and shapes of leaves are key determinants of the efficiency of light capture in plants, and the overall photosynthetic rates of the canopy is a key determinant of yields [1]. The rates and patterns of leaf expansion are governed by the epidermal tissue [2] but understanding how the irreversible growth properties of its constituent jig-saw-puzzle piece cells related to organ level shape change remains as a major challenge.

The epidermal cell, also known as pavement cell, undergoes a dramatic transformation from a slightly irregular polyhedral cell to a highly convoluted and multi-lobed morphology. The interdigitated growth mode is widespread in the plant kingdom [3], and the process by which lobing occurs can reveal how force patterns in the tissue are converted into predictable shape change [4]. To analyze the slow and irreversible growth behavior across wide spatial scales, it is important to track and map lobing events in the epidermal tissue. It has been shown that cell walls perpendicular to the leaf surface, the anticlinal wall as illustrated in Fig. 1, can be used to detect new lobe formations [5], [6].

Time-lapse image stacks from 3D confocal imagery provide a good resource to study the pavement cell growth process, and build the quantitative cell morphogenesis model [7], [4]. 3D confocal microscopy data contain large amount of cell shape and sub-cellular cell wall structure information. Cell analysis requirements include detecting sub-cellular features such as junctions of three cell walls and segments shape of anticlinal cell walls used to detect lobes, all of which depends on accurate segmentation. These sub-cellular features are illustrated in Fig. 1. Currently, these features are usually acquired manually from 3D image stacks. Manual extraction and analysis is not only laborious but also prevents evaluation of large amounts of data necessary to map relationships between lobe formation to leaf growth.

Existing automatic time-lapse cell analysis methods include mainly two steps: (1) Recognizing and localizing cells and cell walls spatially (segmentation) and tracking cells in temporal dimension, (2) cellular/sub-cellular feature extraction. Both of which are existing challenges with

automated analysis systems.

There is an extensive literature on cell segmentation [8], [9], [10], [11], [12], [13], [14], [15], [16], [17] and tracking [18], [19]. In [9], [10], [11], [15] morphological operations are first used to denoise the images followed by watershed or level set segmentation methods to get the final cell segmentation. In [17], the nuclei information is provided for accurate cell segmentation. However, these methods do not provide accurate localization of the cell wall features with only cell boundary information that are needed for quantification. In [8], [13], [14], they focus on improving the cell boundary segmentation accuracy. In [13], [14], they treat the cell segmentation problem as a semantic segmentation problem, using Generative Adversarial Networks (GAN) to differentiate between boundary pixels, cell interior, and background. These methods provide respectable accuracy on cell boundaries but they are not guaranteed to give a closed cell surface. The method proposed in [16] that can provide closed 2D surface while maintaining good 2D cell segmentation boundary results. It is challenging to do the downstream cell analysis such as cell tracking without a closed 3D cell surface. Based on segmentation or detection of cells, [18], [19] rely on Viterbi algorithm to track cells. They require the global optimization which is inefficient to get the cell trajectory.

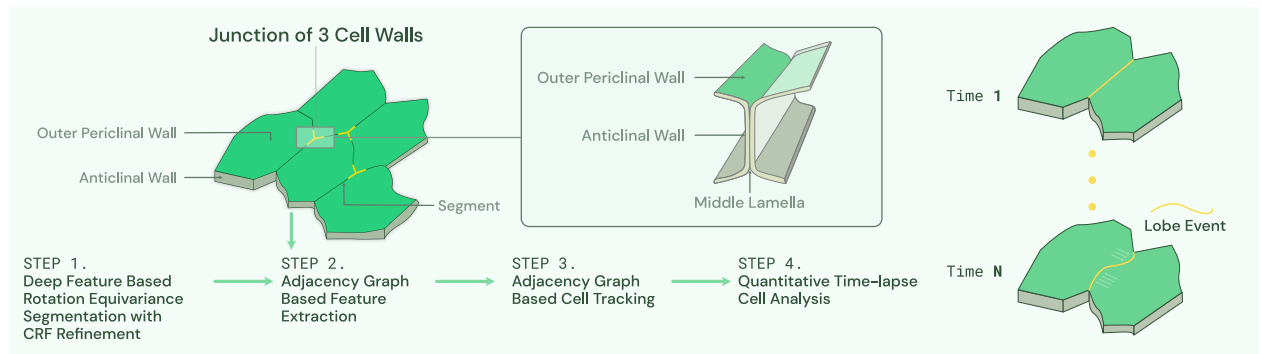


Fig. 1. Workflow of proposed method. Modified from [4]. Given a sequence of 3D image stacks, deep feature based rotation equivariance deep learning model with CRF refinement is used to segment each cell. Then adjacency graph is built based on segmented image and used for sub-cellular feature extraction and tracking. Sub-cellular features such as junction of three cell walls and anticlinical wall segment are illustrated in the figure. Next detected segments will be used in [5] to detect lobes. This paper mainly focuses on Step 1 to Step 3.

This paper presents a robust, time-lapse cell analysis method building upon our earlier work [8]. In [8] we use Conditional Random Field (CRF) to get the improved cell boundaries while

maintaining a closed cell surface. To make the segmentation method more robust to different datasets, we propose a modification to [8] that incorporates rotation invariance in the 3D convolution kernels. A segmentation map labeling each individual cell in the 3D stack is thus created and a cell adjacency graph is constructed from this map. The adjacency graph is an undirected weighted graph with each vertex representing a cell and the weight on the edge representing the minimum distance between two cells. Based on this adjacency graph, sub-cellular features illustrated in Fig. 1 are computed. The cells are tracked by comparing the corresponding adjacency graphs in the time sequence similar to our previous work [20]. Details of the complete workflow will be described in section 3.

We demonstrate the performance of the proposed *segmentation* method on multiple cell wall tagged data sets. The performance of the *tracking* method is demonstrated both on cell wall tagged and nuclei tagged imagery.

In summary, the main contributions of this paper include

- The first deep learning enabled end-to-end fully automated time-lapse 3D cell analysis method
- A new 3D cell segmentation network with rotation equivariance that is robust to different imaging conditions
- A novel graph based method for multiple instance tracking and sub-cellular feature extraction as well as the novel evaluation metrics to evaluate sub-cellular feature extraction accuracy
- We will release a new membrane tagged imagery with partially (expert) annotated sub-cellular features and fully annotated by our computational method.

II. METHOD

Our cell analysis method is illustrated in Fig. 1. First, we segment cells from each image stack in the time sequence. Second, the adjacency graph is built based on segmented images and is used to compute sub-cellular features and cell tracking features. Finally, quantitative measurements of the cell segmentation (cell wall, cell count, cell shape), sub-cellular features (junctions of three

cell walls detection accuracy, anticlinal wall segment shape), and tracking results are provided.

A. Segmentation

We adopt the cell segmentation workflow from [8] with rotation equivariance constrained enforced as shown in Fig.2. 3D U-Net is a reliable method for semantic segmentation specifically for biomedical images, and 2D rotation equivariance has shown its robustness to input image orientation [21]. Therefore, we first use a rotation equivariance 3D U-Net to generate a probability map of each voxel being a cell wall. The full 3D U-Net rotation equivariance is achieved by replacing all convolution layers with rotation-equivariant layers described in the next paragraph. Second, to make sure we can get closed cell surfaces, a 3D watershed algorithm whose seeds are generated automatically is applied to the cell wall probability map, and outputs the initial cell segmentation result. The initial cell segmentation boundary is closed but may not be smooth because watershed segmentation is sensitive to noise. Finally, a conditional random field (CRF) model is used to refine the cell boundaries of the initial cell segmentation. The CRF model takes the cell wall probability map and initial cell segmentation labels as input and outputs a smooth and closed cell wall. In the following section, we will discuss the details of our rotation-equivariant convolution layers and the use CRF to refine the cell segmentation boundary.

3D rotation-equivariant layers are a generalization of convolution layers and are equivariant under general symmetry groups, such as the group of four 90° 2D rotations [21]. The corresponding 3D rotation group has 24 rotations as illustrated in Fig. 2 (A cube has 6 faces and any of those 6 faces can be moved to the bottom, and then this bottom face can be rotated into 4 different positions). To achieve this, convolution operations on feature maps are operating on a group of features which implies that we should have feature channels in groups of 24, corresponding to 24 rotations in the group.

For a given cell wall probability map \mathbf{Q} and cell labels \mathbf{X} , the conditional random field is modeled by the Gibbs distribution,

$$P(\mathbf{X}|\mathbf{Q}) = \frac{1}{Z(\mathbf{Q})} \exp(-E(\mathbf{X}|\mathbf{Q})) \quad (1)$$

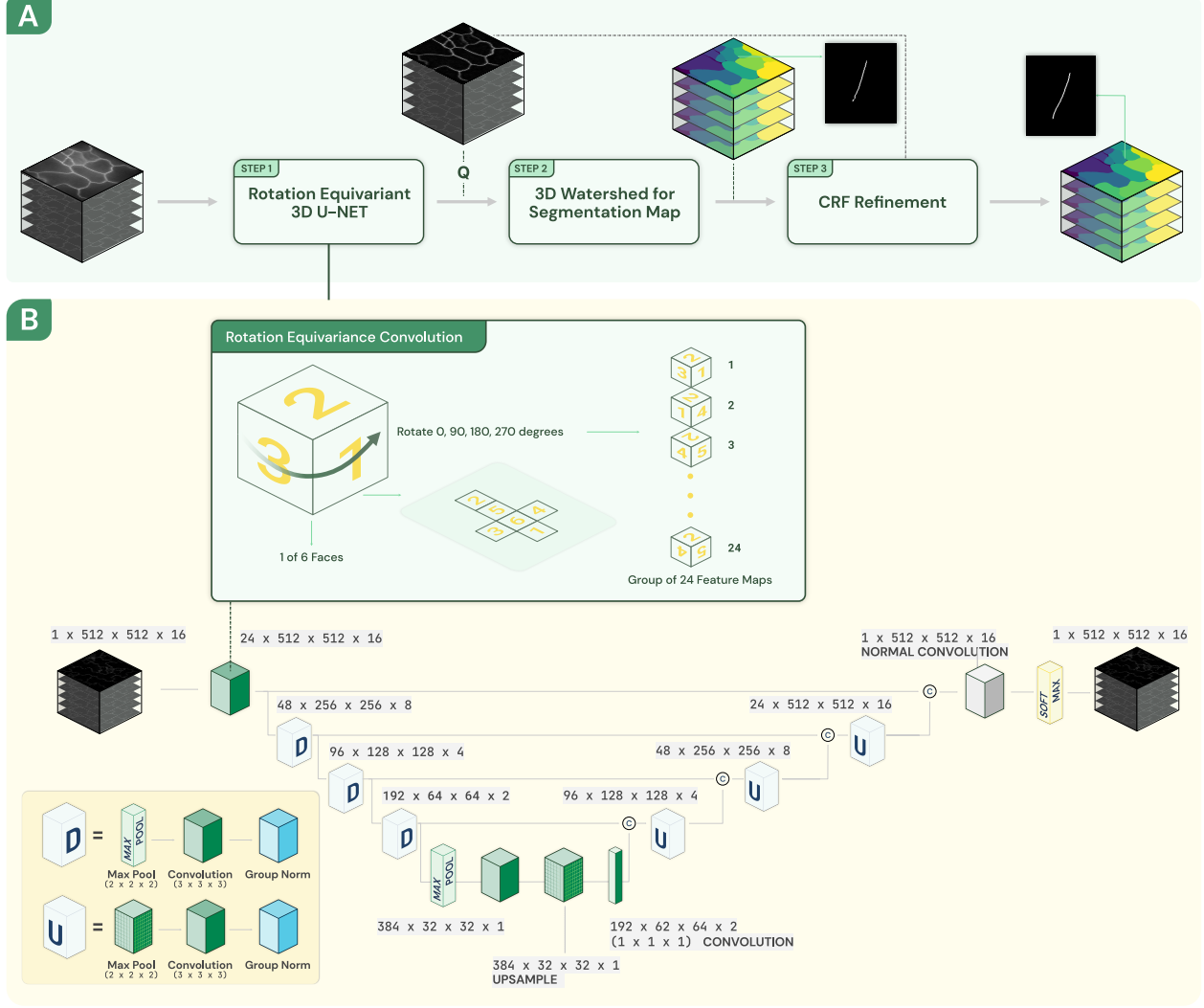


Fig. 2. A. Segmentation workflow includes rotation equivariant 3D U-Net, 3D watershed, and CRF refinement. B. In 3D equivariant U-Net, all convolution layers are rotation equivariant convolution layers. The raw 3D image stack is truncated into 16 slices and then input to 3D equivariant U-Net.

where denominator $Z(\mathbf{Q})$ is the normalization factor. The exponent is the Gibbs energy function and we need to minimize the energy function $E(\mathbf{X})$ to get the final refined label assignments (for notation convenience, all conditioning is omitted from this point for the rest of the paper). In the dense CRF model, the energy function is defined as

$$E(\mathbf{X}) = \sum_i \psi_u(x_i) + \sum_{i < j} \psi_p(x_i, x_j) \quad (2)$$

where i and j are the indices of each voxel which iterate over all voxels in the graph, and x_i and

x_j are the cell labels of vertices i and j . $i, j \in \{1, 2, \dots, N\}$ and N is the total number of voxels in the image stack. $x_i, x_j \in \{0, 1, 2, \dots, L\}$ and L is the total number of cells identified by the watershed method (0 is the background class). The first term of eq. 2, the unary potential, is used to measure the cost of labeling i_{th} voxel as x_i and it is given by $\psi_u(x_i) = -\log P(x_i)$, where $P(x_i)$ is the probability of voxel i having the label x_i . It is initially calculated based on the cell wall probability map \mathbf{Q} and the label image of the watershed \mathbf{X}^0 (The superscript 0 is used to denote the initial cell label assignment after watershed). $P(x_i^0) = 1 - q_i$ if voxel i is inside the cell with label x_i^0 after the watershed or if x_i^0 is the background label, and $P(x_i^0) = 0$ otherwise. q_i is the i_{th} voxel value in the probability map from the rotation equivariant 3D U-Net. $1 - q_i$ represents the probability of voxel being the interior point of the cell. The pairwise potential in eq. 2 takes into account the label of neighborhood voxels to make sure the segmentation label is closed and the boundary is smooth [22]. It is given by:

$$\psi_p(x_i, x_j) = \mu(x_i, x_j) \sum_m w^{(m)} k^{(m)}(\mathbf{f}_i, \mathbf{f}_j) \quad (3)$$

where the penalty term $\mu(x_i, x_j) = 1$ if $x_i \neq x_j$, and $\mu(x_i, x_j) = 0$ otherwise. $w^{(m)}$ is the weight for each segmentation label $m \in \{0, 1, 2, \dots, L\}$, and $k^{(m)}$ is the pairwise kernel term for each pair of voxels i and j in the image stack regardless of their distance that capture the long-distance voxel dependence in the image stack. \mathbf{f}_i and \mathbf{f}_j are feature vectors from the probability map \mathbf{Q} . \mathbf{f}_i incorporates location information of voxel i and the corresponding value in the probability map: $\mathbf{f}_i = \langle \mathbf{p}_i, q_i \rangle$ where $\mathbf{p}_i = \langle x_i, y_i, z_i \rangle$, and x_i, y_i and z_i are the voxel i in coordinates. Specifically, the kernel $k(\mathbf{f}_i, \mathbf{f}_j)$ is defined as

$$k(\mathbf{f}_i, \mathbf{f}_j) = \gamma_1 \exp\left(-\frac{\|\mathbf{p}_i - \mathbf{p}_j\|^2}{2\sigma_\alpha^2} - \frac{\|q_i - q_j\|^2}{2\sigma_\beta^2}\right) + \gamma_2 \exp\left(-\frac{\|\mathbf{p}_i - \mathbf{p}_j\|^2}{2\sigma_\gamma^2}\right) \quad (4)$$

where the first term depends on voxel location and the corresponding voxel value in probability map. The second term only depends on the voxel location. σ_α , σ_β , and σ_γ are the hyper parameters that depends on shape and size of cells in each dataset. Finally, we pick the best label assignment \mathbf{X}^* as the final cell segmentation that minimizes energy function $E(\mathbf{X})$. The efficient CRF

inference algorithm described in [22] is used to find \mathbf{X}^* which is the final cell segmentation mask. In our experiments, the above mentioned CRF regularisation is iteratively applied 2-4 times.

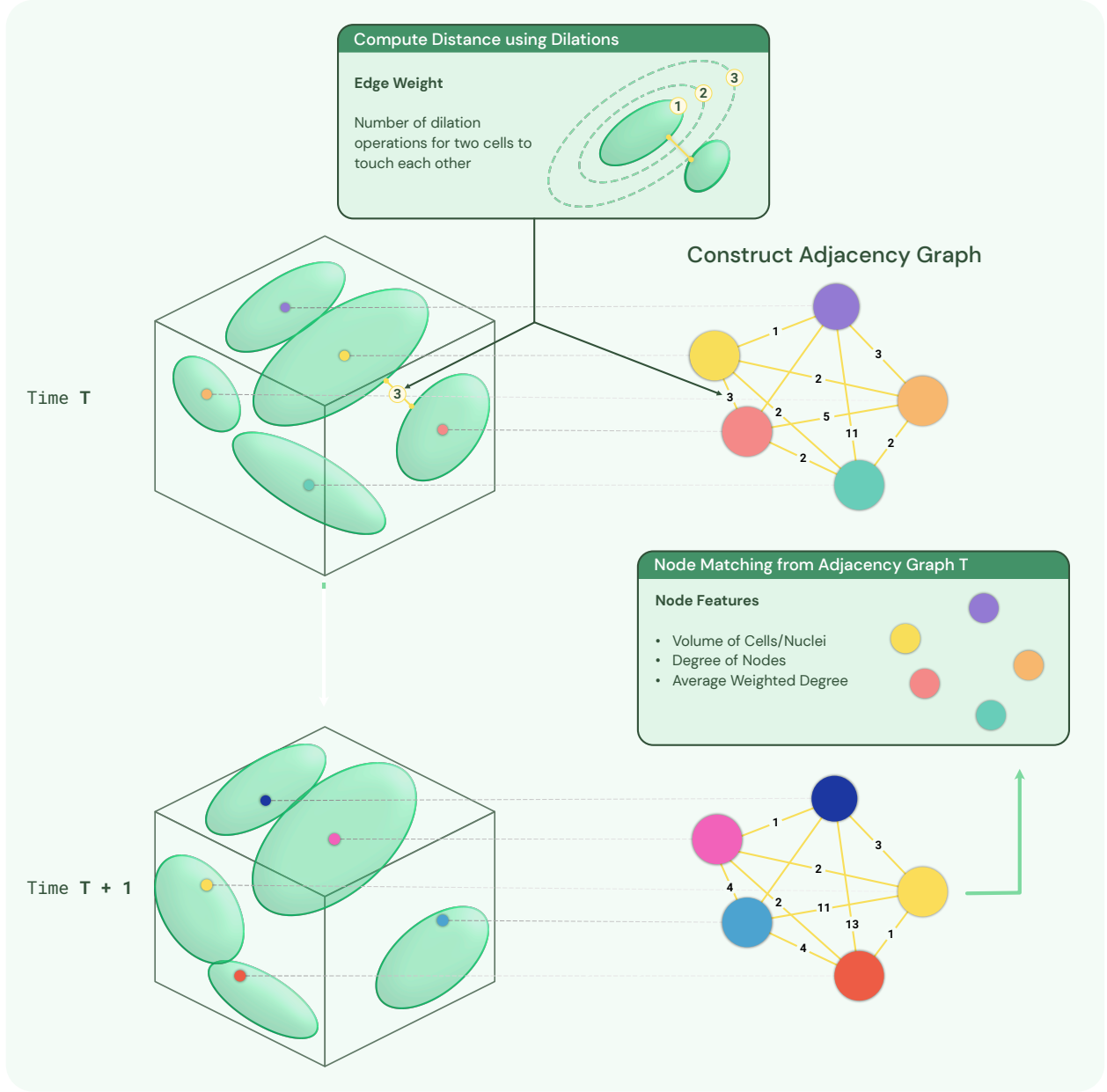


Fig. 3. Constructing adjacency graph from the segmentation image and tracking cells/nuclei in consecutive frames using adjacency graph node features. Color of nodes denote the label/track of the cell/nuclei. Initially, random labels are assigned for each node in the adjacency graph. For T+1 frame, after node matching for time T, track IDs are assigned to each node in T+1.

B. Tracking and Feature Computation

After segmentation of 3D image stacks, the cells are detected and labeled in 3D space. Next, we utilize 3D spatial location of cells to build the adjacency graph for sub-cellular feature extraction and tracking as illustrated in Fig.3.

Adjacency graph $G(V, E)$ is a weighted undirected graph. The vertex $v_i \in V$ represents the i -th cell. For each pair of vertices (v_i, v_j) , there is an edge $e_i \in E$ connecting them. The weight $w_i \in W$ of the edge e_i is the distance between cell i and j . The distance between two cells is computed as the number of morphology dilation operations needed of cells i and j until cell i and j become a single connected component. The details of this adjacency graph construction are given in Algorithm 1 below.

Algorithm 1 Cell Adjacency Graph Construction

```

function CELLADJACENCY(Segmented Image Stack)
  Initiate AdjacentGraph
  Initiate drawboard (the same shape as segmentation) to be 0
  for  $i = 1$  to number of cells do
    for  $j = 1$  to number of cells do
      entry of drawboard is set to 1 if the voxel belong to cell  $i$  or  $j$ 
      if  $i \neq j$  then
        3D dilation of drawboard
        connected component analysis on drawboard
        if number of component is 1 then
          append  $j$  to  $i$ th entry of AdjacentGraph
        end if
      end if
    end for
  end for
end function

```

Sub-cellular Feature Extraction Using Adjacency Graph: Sub-cellular feature extraction is based on the graph representation of the segmented image. To compute the anticlinal wall segments of cell i , we find all neighbor cells of cell i . The neighbor cells \mathbf{N}_i are defined to be all cells that are at a distance 1 from cell i . The anticlinal wall segments is found by collecting all points in the segmentation image shared by cell i and cell j where cell $j \in \mathbf{N}_i$. To compute the junctions of 3 cell walls, we first pick cell $j \in \mathbf{N}_i$. Then the junctions of 3 cell walls is

computed as the points in the segmentation image shared by cell i , cell j , and cell k where cell k is $\mathbf{N}_i \cap \mathbf{N}_j$.

Tracking Using Adjacency Graph: The assumption we make for the cell tracking is that in consecutive image stacks, cells should have similar relative location. For this, we will focus on computing features \mathbf{f}_{loc} that represent cell relative location information derived from the adjacency graph.

Cell location feature vector \mathbf{f}_{loc} is a two dimensional vector (N, D) , where N is the total number of neighbor cells and D is the average distance from all other cells. Consider the adjacency graph $G(V, E)$ of the segmented image stack. For node i in the graph, the location feature vector can be expressed as:

$$\mathbf{f}_{loc}^i = (N, D) = (deg(v_i), wdeg(v_i)) \quad (5)$$

where $v_i \in V$, $deg(v_i)$ is the cardinality of N_i , and $wdeg(v_i)$ is the weighted degree of the vertex v_i . The weighted degree of the vertex v_i is defined as:

$$wdeg(v_i) = \frac{\sum_j w_{ij}}{deg(v_i)} \quad (6)$$

where $deg(v_i)$ represents the degree of the vertex v_i . Then we compute the cell size by counting number of voxels within the cell. Combining the cell location feature and cell size feature, we get the three dimensional feature vector \mathbf{f}_{track} . The details of algorithm used for calculating \mathbf{f}_{track} is described below:

Algorithm 2 Cell Tracking Feature Computation

function CELLTRACKFEATURE(Segmentation and $G(V, E)$)

 Initiate FeatureVector

for $i = 1$ to number of cells **do**

 cell size $S_i = \text{number of voxel inside cell } i \times \text{voxel resolution}$

$wdeg(v_i) = \frac{\sum_j w_{ij}}{deg(v_i)}$

 append $(S_i, deg(v_i), wdeg(v_i))$ to FeatureVector

end for

end function

After computing \mathbf{f}_{track}^i for all nodes in two consecutive frames, we link two nodes from different frames based on the following similarity measurement $sim(i, j)$ defined as

$$sim(i, j) = \frac{|S_{1i} - S_{2j}|}{S_{1i}} + \frac{|deg_1(v_i) - deg_2(v_j)|}{deg_1(v_i)} + \frac{|wdeg_1(v_i) - wdeg_2(v_j)|}{wdeg_1(v_i)} \quad (7)$$

where i and j denote two nodes from two consecutive frames. We define sim so that we can allow different units of entries in \mathbf{f}_{track}^i . We find i^* and j^* that minimizes sim . i^* and j^* are linked only when their sim is below a set threshold value. In our experiments, the threshold we use is between 0.1 to 0.5.

III. DATASET

A. Plasma-membrane Tagged Dataset

Two 3D confocal image stack datasets of fluorescent-tagged plasma-membrane cells are used in this paper. In both datasets, only the plasma-membrane signal is used and is represented by voxels with high intensity values. The first dataset [7] (Dataset 1) consists of a long-term time-lapse from *A. thaliana*'s leaf epidermal tissue that spans over a 12 hour period with a xy-resolution of $0.212\mu m$ and $0.5\mu m$ thick optical sections. There are 5 sequences of image stacks. Each sequence has 9-20 image stacks and each stack has 18 to 25 slices containing one layer of cells, and the dimensions of each slice is 512×512 . Partial ground truth sub-cellular features are provided for this dataset. Details of this dataset are described in Table I.

The second dataset (Dataset 2) contains cells in the shoot apical meristem of 6 *Arabidopsis thaliana* [23]. There are 6 image sequences. Each image sequence has 20 image stacks. In each image stack, there are 129 to 219 slices containing of 3 layers (L) of cells: outer layer (L_1), middle layer (L_2), and deep layer (L_3), and the dimension of each slice is 512×512 . The available resolution of each image in x and y direction are $0.22\mu m$ and in z is about $0.26\mu m$. The ground truth voxel-wise cell labels are provided, and each cell has a unique label. Each cell track also has a unique track ID. Details of this dataset are described in Table II

TABLE I

SINGLE LAYER PAVEMENT CELL DATASET [7]. IT CONSISTS OF A LONG-TERM TIME-LAPSE FROM *A. thaliana*'s LEAF EPIDERMAL TISSUE THAT SPANS OVER A 12 HOUR PERIOD WITH A XY-RESOLUTION OF $0.212\mu m$ AND $0.5\mu m$ THICK OPTICAL SECTIONS. THE TIME STEP IS TWO HOURS FOR SEQUENCE#2 AND IS ONE HOUR FOR ALL OTHER SEQUENCES. ANTICLINAL CELL WALLS ARE PARTIALLY ANNOTATED FOR ALL SEQUENCES. IN ADDITION TO THAT, CELLS ARE PARTIALLY ANNOTATED FOR SEQUENCE#5

Dataset	Number of Time Points	Image Stack Dimension
Sequence 1	20	$512 \times 512 \times 20$
Sequence 2	9	$512 \times 512 \times 18$
Sequence 3	10	$512 \times 512 \times 30$
Sequence 4	13	$512 \times 512 \times 21$
Sequence 5	20	$512 \times 512 \times 25$

TABLE II

MULTI LAYER PAVEMENT CELL DATASET [23]. IT CONTAINS THREE LAYERS OF CELL WALLS IN THE SHOOT APICAL MERISTEM OF *A. thaliana*'s THAT SPANS OVER 80 HOURS WITH WITH A XY-RESOLUTION OF $0.22\mu m$ AND $0.26\mu m$ THICK OPTICAL SECTIONS. THE TIME STEP IS 4 HOURS FOR ALL SEQUENCES AND EACH SEQUENCE HAS 20 FRAMES. CELLS WITH TRACK IDS ARE FULLY PROVIDED.

Dataset	Image Stack Dimension
Sequence 1	$512 \times 512 \times 134$
Sequence 2	$512 \times 512 \times 219$
Sequence 3	$512 \times 512 \times 119$
Sequence 4	$512 \times 512 \times 129$
Sequence 5	$512 \times 512 \times 139$
Sequence 6	$512 \times 512 \times 134$

B. Cell Nuclei Dataset

The 3D time-lapse video sequences of fluorescent nuclei microscopy image of *C.elegans* developing embryo (Dataset 3). Each voxel size is $0.09 \times 0.09 \times 1.0$ in microns. Time points were collected once per minute for five to six hours. There are two videos in the training set and two videos in the testing dataset. Details of this dataset are described in Table III. This dataset is used to evaluate our tracking algorithm performance.

IV. RESULTS

A. Segmentation

We apply our proposed method to the Dataset 1 for the purpose of identifying and analyzing cells based on the segmentation. The segmentation results of our proposed method and other state-

TABLE III
C.ELEGANS DEVELOPING EMBRYO NUCLEI DATASET [24], [25]. THE RESOLUTION OF EACH IMAGE STACK IS $0.09\mu m \times 0.09\mu m \times 1.0\mu m$. SEQUENCE 1 AND 2 ARE TRAINING SET WHICH CONTAINS PARTIAL NUCLEI SEGMENTATION WITH TRACK IDS FOR TRAINING. SEQUENCE 3 AND 4 ARE TESTING SET SO NO ANNOTATIONS AVAILABLE.

Dataset	Time Step (min)	Number of Frames	Image Stack Dimension
Sequence 1	1	250	$512 \times 708 \times 35$
Sequence 2	1.5	250	$512 \times 712 \times 31$
Sequence 3	1	190	$512 \times 712 \times 31$
Sequence 4	1.5	140	$512 \times 712 \times 31$

of-the-art methods are shown in Fig. 4. Our proposed method has visually better segmentation performance with closed cell surface and smooth boundary, and our method is able to identify the inter-cellular spaces and *protrusions* in the 3D cell image stack. For Dataset 1, we do not have full cell annotations, so we only evaluate the cell counting accuracy on this dataset.

TABLE IV
CELL COUNTING ACCURACY FOR DIFFERENT METHODS. FOR EACH TIME SEQUENCE, THERE IS A FIXED NUMBER OF CELLS. DUE TO SEGMENTATION ERROR, THE ALGORITHMS CAN GENERATE DIFFERENT NUMBER OF CELLS FOR DIFFERENT TIME POINTS OF THE SEQUENCE. IN THE TABLE, WE SHOWED AVERAGE AND STANDARD DEVIATION OF NUMBER OF DETECTION CELLS FOR THE WHOLE SEQUENCE

Sequence	Ground truth	ACME[10]	MARS [11]	Supervoxel Method [12]	Our method
Sequence 1	23	21.5 ± 3.2	25.5 ± 2.2	24 ± 1.1	23.5 ± 0.9
Sequence 2	30	41.1 ± 3.1	35.1 ± 2.8	32 ± 2.1	30.1 ± 0.8
Sequence 3	25	22.6 ± 2.1	27.5 ± 3.2	24 ± 1.5	25 ± 0.5
Sequence 4	18	18.8 ± 1.2	18.5 ± 1.2	18.2 ± 1.2	18 ± 0.6
Sequence 5	28	31.5 ± 2.9	24.5 ± 2.3	26.2 ± 1.1	27.8 ± 1

For each sequence, there are a fixed number of cells for all time points. Therefore, we want segmentation algorithms to generate average cell counting results close to ground truth counting numbers, and the variance of counting results for one sequence should be as small as possible. Details of the cell counting results are in Table IV. Clearly, our method has the best cell counting performance.

In order to verify if the output of the segmentation can be used for time lapse sequence analysis, we calculate basic cell shape information from the maximum area plane of the cells to compare with the expert annotations. The maximum area plane of a cell is the image plane

which has the largest cell area across all z-slices. The shape information includes area, perimeter, circularity, and solidarity. Fig. 5 shows the comparison. Note that not all cells are annotated so that some cell comparisons are missed. The average shape difference is 4.5 percent and the largest shape difference is within 10 percent.

Next, we apply our cell segmentation method on Dataset 2. Half of the L_1 layer of the training set is used to train the 3D U-Net, and the remaining L_1 , L_2 and L_3 layers of the testing set are used to evaluate the segmentation performance of the proposed algorithm. To measure the boundary segmentation accuracy, for each labeled cell wall voxel in ground truth, we view it as the binary detection problem. If there is a detected boundary voxel by any boundary detection algorithm within 5 voxels of a ground truth boundary voxel, then it is a correct detection. If there is not any detected boundary voxel by algorithms within 5 voxels of a ground truth boundary voxel, then it is a miss detection. If there is a detected boundary voxel by algorithms within 5 voxels of a voxel that is not ground truth boundary voxel, then it is a miss detection. Based on this binary detection, we calculate the boundary segmentation precision, recall, and F-score. Table V to VII shows the comparison of the final segmentation boundary result using our proposed method and other methods including ACME [10], MARS [11] and a supervoxel-based algorithm [12] on L_1 to L_3 respectively. In terms of cell wall accuracy, our model shows at least 0.03 improvement in the F-score measure on average in terms of cell wall segmentation accuracy.

It is noted that the average segmentation time of our proposed model is significantly shorter compared to the supervoxel-based method [12]. Our proposed method takes approximately 0.8 seconds to segment one 512×512 image slice on average, whereas supervoxel-based method takes approximately 6 seconds on a NVIDIA GTX Titan X with an Intel Xeon CPU E5-2696 v4 @ 2.20GHz.

B. Tracking and Feature Extraction

We apply our whole workflow on Dataset 1 to extract sub-cellular features like anticlinal wall segments and junctions of 3 cell walls. Qualitative results of the extracted sub-cellular features

TABLE V

3D SEGMENTATION PERFORMANCE ON L_1 . IF THERE IS A DETECTED BOUNDARY VOXEL BY ALGORITHMS WITHIN 5 VOXELS OF A GROUND TRUTH BOUNDARY VOXEL, THEN IT IS A CORRECT DETECTION. IF THERE IS NOT ANY DETECTED BOUNDARY VOXEL BY ALGORITHMS WITHIN 5 VOXELS OF A GROUND TRUTH BOUNDARY VOXEL, THEN IT IS A MISS DETECTION. IF THERE IS A DETECTED BOUNDARY VOXEL BY ALGORITHMS WITHIN 5 VOXELS OF A VOXEL THAT IS NOT GROUND TRUTH BOUNDARY VOXEL, THEN IT IS A MISS DETECTION. SAME EVALUATION METRIC FOR L_2 AND L_3

Algorithm	Precision	Recall	F-Score
ACME [10]	0.805	0.966	0.878
MARS [11]	0.910	0.889	0.899
Supervoxel method [12]	0.962	0.932	0.947
our method	0.961	0.973	0.967

TABLE VI

3D SEGMENTATION PERFORMANCE ON L_2

Algorithm	Precision	Recall	F-Score
ACME [10]	0.775	0.980	0.866
MARS [11]	0.921	0.879	0.900
Supervoxel method [12]	0.910	0.932	0.921
our method	0.955	0.971	0.963

TABLE VII

3D SEGMENTATION PERFORMANCE ON L_3

Algorithm	Precision	Recall	F-Score
ACME [10]	0.745	0.976	0.845
MARS [11]	0.909	0.879	0.894
Supervoxel method [12]	0.982	0.881	0.929
our method	0.955	0.942	0.949

are shown in Fig. 6.

The quantitative measurement of accuracy of junctions of 3 cell walls is also provided. We compare our results with 3D corner detection based method [26] on the raw image stack, and applying our 3 cell wall junction detection method using the segmentation image from other state-of-the-art methods [10], [11], [12]. The 3 cell wall junction detection results are shown in Table VIII. If 3 cell wall junctions are detected within 5 voxels of a ground truth 3 cell wall junction, it is a correct detection. Then we define false positive (FP), and false negative (FN) based on the binary detection of 3 cell walls junction. The error (E) is defined by the summation of FP and FN and normalized by total number of true 3 cell wall junctions. The results in the

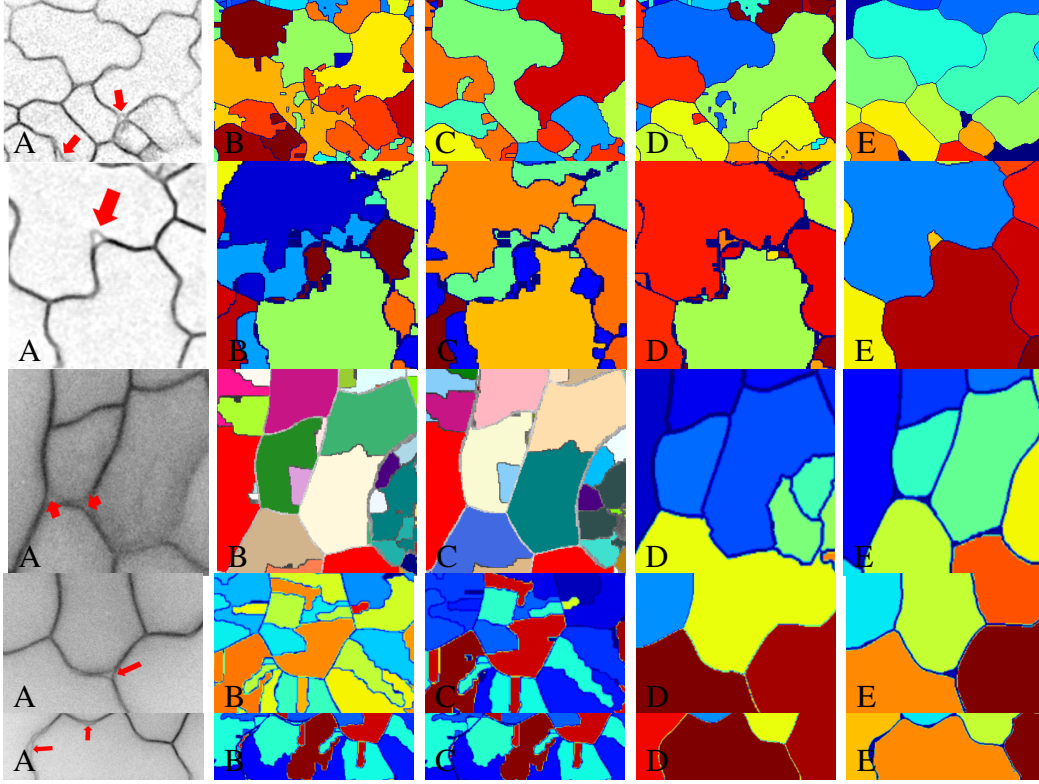


Fig. 4. The figure shows the segmentation results of the cell image with inter-cellular space or *protrusion* indicated by a red arrow. (A) Inverted raw image in xy orientation, (B) MARS, (C) ACME, (D) supervoxel-based method, (E) proposed method.

table VIII are average values across all image stacks. From the table, we can see our method has the best 3 cell wall junction detection accuracy in terms of E. Compared to the method that directly computes 3 cell wall junctions from raw image, our method has significantly better performance in terms of FP. This is because not all corner points are junctions of three cell walls. For example, corner detection based method gives false positive in the case shown in Fig. 7. Our graph based image feature extraction model not only uses low level image features but also some semantic information.

The anticlinal wall segment is defined by two neighboring junctions of 3 cell walls are also computed. The partial annotation of such segments are provided. We would like to note that such manual annotations are very labor intensive and it is impractical to annotate all anticlinal cell wall segments (see Fig 1) even in a single 3D volume. The practical difficulties include lack of support for 3D visualization and annotation tools for tracing. The ground truth segments were

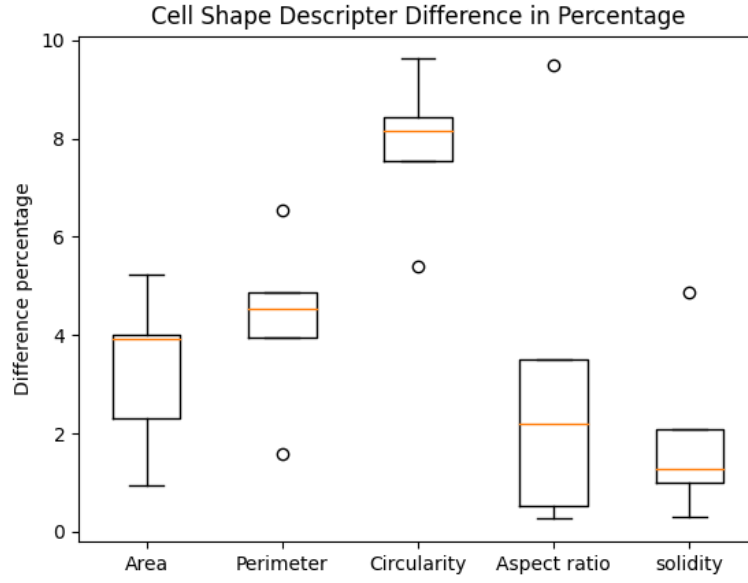


Fig. 5. 3D segmentation evaluation using cell shape descriptor including area, perimeter, circularity, aspect ratio, and solidity (ratio between cell area and its convex hull area). The difference is in terms of percentage.

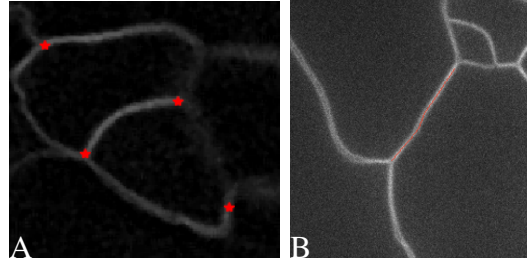


Fig. 6. A: Extracted junctions of three cell walls, B: Extracted anticlinal wall segment.

annotated by going through each slice in the image stack, finding the approximate slice where neighboring cell walls touch, and then tracing the segment in that single slice. Each segment in the ground truth is represented by a collection of coordinates of the segment in that image slice. Note that different segments can be on different slices. In contrast, each of our computed segments can span multiple Z slices, hence providing a more accurate 3D representation than is manually feasible. This also makes it challenging to compare the manual ground truth with the computed results.

We define a set of evaluation metrics to evaluate how accurate our extracted anticlinal wall

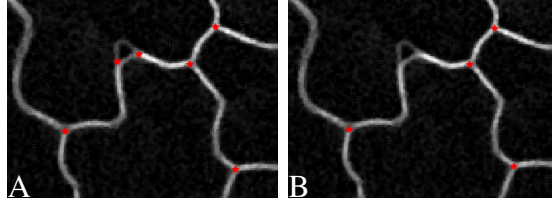


Fig. 7. Example of computing 3 cell wall junctions from raw image (A), and (B) using our method.

TABLE VIII
QUANTITATIVE ANALYSIS ON ERROR OF JUNCTIONS OF THREE CELL WALLS. FP IS AVERAGE NUMBER OF FALSE POSITIVE 3 CELL WALL DETECTION FOR ONE 3D IMAGE STACK. FN IS AVERAGE NUMBER OF FALSE NEGATIVE 3 CELL WALL DETECTION FOR ONE 3D IMAGE STACK. E IS THE SUMMATION OF FP AND FN AND NORMALIZED BY TOTAL NUMBER OF TRUE 3 CELL WALL JUNCTIONS

Algorithm	FP	FN	E
Corner Detection[26]	6.23	1.98	0.15
ACME [10]	10.33	2.11	0.23
MARS [11]	12.54	1.11	0.26
Supervoxel method [12]	3.27	2.68	0.11
Our Method	1.21	1.77	0.05

segments are compared to their partial annotations. Given the ground truth segment and the corresponding computed segment, the following evaluation metrics are computed:

- 1) End-point Displacement error (EDE) in the end points of the two segments;
- 2) Fréchet distance (FD) between the two segments. FD is a measure of shape similarity of two curves and it takes into account the location and ordering of points along the curves. Mathematically, consider two curves P and Q , FD $F(P, Q)$ between them is defined in the following equation

$$F(P, Q) = \inf_{\alpha, \beta} \max_{t \in [0, 1]} d(P(\alpha(t)), Q(\beta(t))) \quad (8)$$

where d is the Euclidean distance, $\alpha : [0, 1] \rightarrow [0, m]$, $\beta : [0, 1] \rightarrow [0, n]$ are all monotone parameterization of $[0, m]$ and $[0, n]$ respectively. m and n are length of P and Q .

- 3) Length difference (LD), absolute difference in lengths between the two segments

TABLE IX
ANTICLINAL CELL WALL SEGMENT EVALUATION ON DATASET 1 USING EDE, FD, LD, DP

Sequence	EDE	FD	LD	DP
Sequence 1	2.80	4.00	2.32	2.90
Sequence 2	6.40	8.40	4.19	6.10
Sequence 3	3.05	3.9	1.74	2.4
Sequence 4	3.02	3.70	2.24	2.3
Sequence 5	2.33	3.40	2.11	2.10

4) Percentage difference in length (DP), length difference normalized by ground truth length.

Average EDE between the results using our method and the ground truth is 3.03 voxels, average FD is 3.7 voxels, average LD is 2.24 voxels, and average DP is 2.3 percent. Evaluation results of different time series are shown in Table IX and evaluation result for each segment is in the supplemental materials.

We also apply our tracking method on Dataset 2 and Dataset 3. Table X shows the quantitative comparison of our method with other state-of-the-art cell/nuclei tracking methods. The evaluation metric we use is tracking accuracy (TRA), proposed in [27]. TRA measures how accurately each cell/nuclei is identified and followed in successive image stacks of the sequence. Ground truth tracking results and tracking results generated from algorithms are viewed as two acyclic oriented graphs and TRA measures the number of operations needed to modify one graph to another. More specifically, TRA is defined on Acyclic Oriented Graph Matching (AOGM) as

$$\text{TRA} = 1 - \frac{\min(\text{AOGM}, \text{AOGM}_0)}{\text{AOGM}_0} \quad (9)$$

where AOGM_0 is the AOGM value required for creating the reference graph from scratch. TRA ranges between 0 to 1 (1 means perfect tracking). Our method shows a rough 0.05 TRA measurement improvement on Dataset 2. To demonstrate the robustness of our tracking method, we also apply it on Dataset 3, a cell nuclei dataset, and achieve a TRA of 0.895 which is comparable to state-of-the-art tracking methods on IEEE ISBI CTC2020 cell tracking challenge.

State-of-the-art methods ([28] and [29]) are based on the traditional Viterbi cell tracking algorithm whose complexity is $\mathcal{O}(TM^4)$ where T is the length of the sequence and M is the maximum number of cells/nuclei. In contrast, the complexity of our method is $\mathcal{O}(TM^2)$. Sequence 1 and 2 are the training data released from the challenge and we run the state-of-the-art methods on the individual sequence to get TRA evaluation metric. Sequence 3 and 4 are testing data that is not published by the challenge and TRA values are given by the challenge organization.

TABLE X
CELL TRACKING PERFORMANCE ON DATASET 2 AND DATASET 3

Dataset 2	Viterbi Tracker[18]	Cell Proposal[30]	Our method
Sequence 1	0.513	0.492	0.571
Sequence 2	0.520	0.512	0.593
Sequence 3	0.488	0.532	0.581
Sequence 4	0.533	0.498	0.566
Sequence 5	0.542	0.525	0.602
Sequence 6	0.518	0.542	0.544
Dataset 3	KIT-Sch-GE [28]	KTH-SE [29]	Our method
Sequence 1	0.903	0.942	0.931
Sequence 2	0.906	0.893	0.912
Sequence 3 and 4	0.886	0.945	0.895

V. CONCLUSION

In this paper, we present an end-to-end workflow for extracting quantitative information from 3D time-lapse imagery. The workflow includes 3D segmentation, tracking, and sub-cellular feature extraction. The 3D segmentation pipeline utilizes deep learning models with rotation equivariance. Then an adjacency graph is built for cell tracking and sub-cellular feature extraction. We demonstrate the performance of our model on multiple cell/nuclei datasets. In addition, we also curate a new pavement cell dataset with partial expert annotations that will be made available to researchers.

The proposed segmentation method is implemented as a computational module in BisQue [31], [32]. The BisQue platform `bisque2.ece.ucsb.edu` helps researchers organize, analyze, visualize, annotate, and share multi-dimensional, multimodal imaging data [31], [32]. Further, BisQue enables reproducible image analysis and provenance tracking of the computations on the data. The segmentation module in BisQue is referred to as CelLECT2.0.

Users can run the CelLECT2.0 module using the following steps: (1) Navigate to BisQue on their web browser and create an account, (2) Upload their own data in TIFF format or use suggested example dataset, (3) Select an uploaded TIFF image or use our example, (4) Select Run and the BisQue service will compute the segmentation results and display it in the browser. The runtime for a $512 \times 512 \times 18$ image is approximately one minute using a CPU node with a 24 core Xeon processor and 128GB of RAM. We provide screenshots of these steps in the supplemental materials.

VI. ACKNOWLEDGEMENT

This work was supported by the National Science Foundation award No.1715544 to DBS and BSM, and the National Science Foundation SSI award No.1664172 to BSM.

VII. AUTHOR CONTRIBUTIONS

JJ designed and carried out the overall computer vision method pipeline including segmentation, tracking, and feature extraction, helped implement software into Bisque and drafted manuscript. AK dockerized the segmentation code, integrated the module into BisQue, and helped manuscript preparation. SS helped get cell nuclei tracking results, and helped manuscript preparation. SB obtained membrane tagged cell dataset, manually segmented sub-cellular features, and helped prepare the manuscript. MG helped visualization of segmentation results on BisQue and optimized adjacency graph computation. DBS coordinated membrane tagged cell dataset acquisition, helped analyzed the data, and reviewed manuscript. BSM coordinated the overall design, development and evaluations of the image processing methods, and helped prepare the manuscript.

VIII. DATA AVAILABILITY

The code is available on GitHub. Dataset 1, Dataset 2, and Dataset 3 analyzed during the paper are available in the repository, Dataset 1, Dataset 2, and Dataset 3 separately.

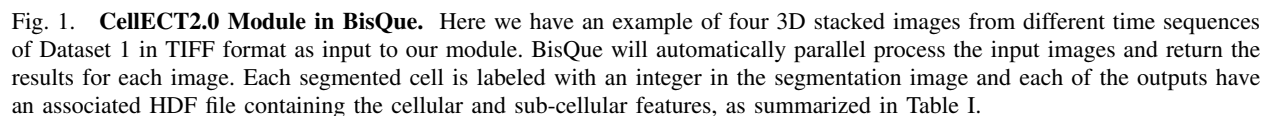
REFERENCES

- [1] X.-G. Zhu, S. P. Long, and D. R. Ort, “Improving photosynthetic efficiency for greater yield,” *Annual review of plant biology*, vol. 61, pp. 235–261, 2010.
- [2] S. Savaldi-Goldstein, C. Peto, and J. Chory, “The epidermis both drives and restricts plant shoot growth,” *Nature*, vol. 446, no. 7132, pp. 199–202, 2007.
- [3] R. V. Vőfély, J. Gallagher, G. D. Pisano, M. Bartlett, and S. A. Braybrook, “Of puzzles and pavements: a quantitative exploration of leaf epidermal cell shape,” *New Phytologist*, vol. 221, no. 1, pp. 540–552, 2019.
- [4] S. A. Belteton, W. Li, M. Yanagisawa, F. A. Hatam, M. I. Quinn, M. K. Szymanski, M. W. Marley, J. A. Turner, and D. B. Szymanski, “Real-time conversion of tissue-scale mechanical forces into an interdigitated growth pattern,” *Nature Plants*, vol. 7, no. 6, pp. 826–841, 2021.
- [5] T.-C. Wu, S. A. Belteton, J. Pack, D. B. Szymanski, and D. M. Umlis, “Lobefinder: A convex hull-based method for quantitative boundary analyses of lobed plant cells,” *Plant Physiology*, vol. 171, no. 4, pp. 2331–2342, 2016. [Online]. Available: <http://www.plantphysiol.org/content/171/4/2331>
- [6] B. Möller, Y. Poeschl, R. Plötner, and K. Bürstenbinder, “Pacequant: a tool for high-throughput quantification of pavement cell shape characteristics,” *Plant physiology*, vol. 175, no. 3, pp. 998–1017, 2017.
- [7] S. A. Belteton, M. G. Sawchuk, B. S. Donohoe, E. Scarpella, and D. B. Szymanski, “Reassessing the roles of pin proteins and anticlinal microtubules during pavement cell morphogenesis,” *Plant Physiology*, vol. 176, no. 1, pp. 432–449, 2018.
- [8] J. Jiang, P.-Y. Kao, S. A. Belteton, D. B. Szymanski, and B. S. Manjunath, “Accurate 3d cell segmentation using deep features and crf refinement,” in *2019 IEEE International Conference on Image Processing (ICIP)*, Sep. 2019, pp. 1555–1559.
- [9] J. Stegmaier, F. Amat, W. C. Lemon, K. McDole, Y. Wan, G. Teodoro, R. Mikut, and P. J. Keller, “Real-time three-dimensional cell segmentation in large-scale microscopy data of developing embryos,” *Developmental cell*, vol. 36, no. 2, pp. 225–240, 2016.
- [10] K. R. Mosaliganti, R. R. Noche, F. Xiong, I. A. Swinburne, and S. G. Megason, “Acme: automated cell morphology extractor for comprehensive reconstruction of cell membranes,” *PLoS computational biology*, vol. 8, no. 12, p. e1002780, 2012.
- [11] R. Fernandez, P. Das, V. Mirabet, E. Moscardi, J. Traas, J.-L. Verdeil, G. Malandain, and C. Godin, “Imaging plant growth in 4d: robust tissue reconstruction and lineaging at cell resolution,” *Nature methods*, vol. 7, no. 7, pp. 547–553, 2010.
- [12] J. Stegmaier, T. V. Spina, A. X. Falcão, A. Bartschat, R. Mikut, E. Meyerowitz, and A. Cunha, “Cell segmentation in 3d confocal images using supervoxel merge-forests with cnn-based hypothesis selection,” in *Biomedical Imaging (ISBI 2018), 2018 IEEE 15th International Symposium on*. IEEE, 2018, pp. 382–386.

- [13] H. Tsuda and K. Hotta, "Cell image segmentation by integrating pix2pixs for each class," in *The IEEE Conference on Computer Vision and Pattern Recognition (CVPR) Workshops*, June 2019.
- [14] M. Majurski, P. Manescu, S. Padi, N. Schaub, N. Hotaling, C. Simon Jr, and P. Bajcsy, "Cell image segmentation using generative adversarial networks, transfer learning, and augmentations," in *Proceedings of the IEEE/CVF Conference on Computer Vision and Pattern Recognition Workshops*, 2019, pp. 0–0.
- [15] D. L. Delibaltov, U. Gaur, J. Kim, M. Kourakis, E. Newman-Smith, W. Smith, S. A. Belteton, D. B. Szymanski, and B. Manjunath, "Cellec: cell evolution capturing tool," *BMC bioinformatics*, vol. 17, no. 1, p. 88, 2016.
- [16] C. Stringer, T. Wang, M. Michaelos, and M. Pachitariu, "Cellpose: a generalist algorithm for cellular segmentation," *Nature methods*, vol. 18, no. 1, pp. 100–106, 2021.
- [17] W. Han, A. M. Cheung, M. J. Yaffe, and A. L. Martel, "Cell segmentation for immunofluorescence multiplexed images using two-stage domain adaptation and weakly labeled data for pre-training," *Scientific Reports*, vol. 12, no. 1, pp. 1–14, 2022.
- [18] D. E. Hernandez, S. W. Chen, E. E. Hunter, E. B. Steager, and V. Kumar, "Cell tracking with deep learning and the viterbi algorithm," in *2018 International Conference on Manipulation, Automation and Robotics at Small Scales (MARSS)*, July 2018, pp. 1–6.
- [19] Z. Zhou, F. Wang, W. Xi, H. Chen, P. Gao, and C. He, "Joint multi-frame detection and segmentation for multi-cell tracking," in *Image and Graphics*. Cham: Springer International Publishing, 2019, pp. 435–446.
- [20] S. Shailja, J. Jiang, and B. Manjunath, "Semi supervised segmentation and graph-based tracking of 3d nuclei in time-lapse microscopy," in *2021 IEEE 18th International Symposium on Biomedical Imaging (ISBI)*. IEEE, 2021, pp. 385–389.
- [21] B. Chidester, T.-V. Ton, M.-T. Tran, J. Ma, and M. N. Do, "Enhanced rotation-equivariant u-net for nuclear segmentation," in *The IEEE Conference on Computer Vision and Pattern Recognition (CVPR) Workshops*, June 2019.
- [22] P. Krähenbühl and V. Koltun, "Efficient inference in fully connected crfs with gaussian edge potentials," *Advances in neural information processing systems*, vol. 24, 2011.
- [23] S. H. Jonsson, L. Willis, and Y. Refahi, "Research data supporting cell size and growth regulation in the arabidopsis thaliana apical stem cell niche," *[Dataset]*, 2017.
- [24] V. Ulman, M. Maška, K. E. Magnusson, O. Ronneberger, *et al.*, "An objective comparison of cell-tracking algorithms," *Nature methods*, vol. 14, no. 12, pp. 1141–1152, 2017.
- [25] S. D. Maška M, Ulman V *et al.*, "A benchmark for comparison of cell tracking algorithms," *Bioinformatics*, vol. 30, no. 11, pp. 1609–1617, 02 2014. [Online]. Available: <https://doi.org/10.1093/bioinformatics/btu080>
- [26] B. Zhong, K.-K. Ma, and W. Liao, "Scale-space behavior of planar-curve corners," *IEEE Transactions on Pattern Analysis and Machine Intelligence*, vol. 31, no. 8, pp. 1517–1524, 2008.
- [27] V. Ulman, M. Maška, K. E. Magnusson, O. Ronneberger, C. Haubold, N. Harder, P. Matula, P. Matula, D. Svoboda, M. Radojevic, *et al.*, "An objective comparison of cell-tracking algorithms," *Nature methods*, vol. 14, no. 12, pp. 1141–1152, 2017.
- [28] K. Löffler and T. Scherr, "KIT-Sch-GE," *Cell Tracking Challenge*, 2020.
- [29] K. E. Magnusson, J. Jaldén, P. M. Gilbert, and H. M. Blau, "Global linking of cell tracks using the Viterbi algorithm," *IEEE transactions on medical imaging*, vol. 34, no. 4, pp. 911–929, 2014.

- [30] S. U. Akram, J. Kannala, L. Eklund, and J. Heikkilä, “Cell tracking via proposal generation and selection,” *ArXiv*, vol. abs/1705.03386, 2017.
- [31] K. Kvilekval, D. Fedorov, B. Obara, A. Singh, and B. Manjunath, “Bisque: a platform for bioimage analysis and management,” *Bioinformatics*, vol. 26, no. 4, pp. 544–552, 2010.
- [32] M. I. Latypov, A. Khan, C. A. Lang, K. Kvilekval, A. T. Polonsky, M. P. Echlin, I. J. Beyerlein, B. Manjunath, and T. M. Pollock, “Bisque for 3d materials science in the cloud: microstructure–property linkages,” *Integrating Materials and Manufacturing Innovation*, vol. 8, no. 1, pp. 52–65, 2019.

I. SEGMENTATION AND SUB-CELLULAR FEATURE EXTRACTION FROM BISQUE



The full cellular and sub-cellular results for this image stack can be accessed [here](#).

TABLE I
CELLULAR AND SUB-CELLULAR FEATURES PROVIDED BY BISQUE

Different features	Example Values or Explanation
Cell Volume	number of voxels inside a cell, for example, 358,445
Neighboring (Adjacent) cells	for example, cells 1,3,11,14 are neighboring cells of cell 2
3D cell surface	list of coordinates of surface of points for one cell
Three cell wall junction points	for example, junction point of cell 2,3,11 is (12,207)
Cell Center	for example, center of cell 2 is (8,61,8)
Segments	list of coordinates of points along that segment

II. SEGMENTS EVALUATION

Some examples of segments evaluation are summarized in Table II. The evaluation metrics include: Euclidean error of start (end) points of segments, Fréchet Distance, and length difference of segments. In Table II, the first column is segment ID. Segment ID includes two parts: Sequence ID and the segment ID within the sequence. Sequence ID starts with “LGMTPM” and ends with a 2-digit number to differentiate different sequences. Segment ID contains information about which frame this segment comes from. For example, “LGMTPM01 Seg03T28” means this segment comes from frame 28 of sequence 01.

Detailed comparison results are in the `segments.xlsx` file.

TABLE II
SEGMENTS EVALUATION RESULTS. THE RESULTS INCLUDE SEGMENTS' END POINTS LOCATION ACCURACY, SEGMENTS LENGTH ACCURACY, AND FRECHET DISTANCE FOR SEGMENTS SHAPE ACCURACY

	detected start point x	detected start point y	detected start point z	detected end point x	detected end point y	detected end point z	GT start point x	GT start point y	GT end point x	GT end point y	euclidean distance error start point	euclidean distance error end point	Frechet Distance	GT Length	Detected Length	difference	% change
LGMTPM01 Seg03T28	391	215	3	485	203	3	392.7	216.2	481.8	203.3	2.0	3.2	3.9	95.1	93.4	1.7	1.8
LGMTPM01 Seg06T24	121	144	4	195	142	5	124.9	145.3	196.0	139.0	4.1	3.2	4.1	85.6	87.2	1.6	1.9
LGMTPM01 Seg02T01	169	356	2	234	360	4	172.8	358.3	233.3	360.3	4.5	0.7	4.5	66.6	70.3	3.6	5.4
LGMTPM01 Seg05T01	303	274	6	350	320	2	303.5	273.3	346.8	320.0	0.9	3.3	3.3	70.7	72.9	2.2	3.1
LGMTPM01 Seg08T01	200	59	1	299	82	2	204.3	59.8	297.3	81.8	4.3	1.8	4.3	100.6	98.1	2.4	2.4
LGMTPM02 Seg05T23	207	138	4	217	77	5	210.2	143.8	213.3	82.0	6.6	6.2	8.4	68.9	73.1	4.2	6.1
LGMTPM03 Seg02T32	178	212	4	246	183	4	182.7	212.3	243.7	182.7	4.7	2.4	4.1	77.8	80.3	2.5	3.2
LGMTPM04 Seg03T17	286	327	5	328	392	7	289.7	329.3	325.2	395.7	4.3	4.6	4.7	85.2	83.3	2.0	2.3
LGMTPM05 Seg03T01	45	220	3	145	224	5	48.8	219.3	145.3	220.3	3.8	3.8	3.7	106.5	108.1	1.6	1.5
LGMTPM05 Seg03T02	11	198	2	100	200	4	13.5	196.5	101.5	198.0	2.9	2.5	3.0	98.0	100.0	2.0	2.0
LGMTPM05 Seg03T01	12	201	3	100	200	5	13.0	202.5	102.3	203.5	1.8	4.2	2.9	99.3	97.0	2.2	2.3
LGMTPM05 Seg03T03	13	200	10	103	200	8	14.0	199.8	102.5	201.0	1.0	1.1	3.6	98.5	102.1	3.6	3.7
LGMTPM05 Seg03T04	17	208	9	102	211	7	15.5	205.5	104.5	206.3	2.9	5.4	3.7	99.0	103.1	4.1	4.1
LGMTPM05 Seg03T05	16	210	8	105	212	8	15.8	209.3	105.3	210.3	0.8	1.8	3.5	99.5	101.2	1.7	1.7
LGMTPM05 Seg03T06	18	184	6	105	185	8	17.0	182.5	106.8	184.0	1.8	2.0	3.2	95.8	98.1	2.3	2.4
LGMTPM05 Seg03T07	19	216	7	104	218	9	17.0	215.8	106.8	216.5	2.0	3.1	3.3	99.8	101.2	1.5	1.5
LGMTPM05 Seg03T08	18	221	6	105	221	8	17.0	220.0	106.5	220.8	1.4	1.5	3.6	99.6	102.3	2.7	2.7
LGMTPM05 Seg03T09	18	200	6	110	201	7	19.3	199.0	109.5	199.8	1.6	1.3	3.1	100.3	101.3	1.0	1.0
LGMTPM05 Seg03T10	24	192	5	110	195	7	22.0	193.5	112.3	194.0	2.5	2.5	3.3	100.3	102.3	2.1	2.0
LGMTPM05 Seg03T11	23	197	6	115	200	9	22.0	196.9	113.3	197.8	1.0	2.9	3.4	101.3	101.2	0.1	0.1
LGMTPM05 Seg03T12	25	200	11	117	199	9	25.0	198.5	115.3	198.3	1.5	1.8	3.3	100.3	101.4	1.0	1.0
LGMTPM05 Seg03T13	25	201	10	114	198	8	24.3	197.3	116.3	200.5	3.8	3.4	3.2	102.1	104.3	2.2	2.2
LGMTPM05 Seg03T14	27	200	9	118	200	7	25.5	198.5	118.0	200.3	2.1	0.3	3.6	102.5	103.3	0.7	0.7
LGMTPM05 Seg03T15	26	199	7	119	202	7	29.0	197.8	122.5	198.3	3.3	5.1	3.2	103.5	101.5	2.0	2.0
LGMTPM05 Seg03T16	29	195	11	122	199	12	31.3	196.3	125.0	197.8	2.6	3.3	3.4	103.8	100.3	3.5	3.3
LGMTPM05 Seg03T17	32	220	10	126	220	11	33.8	221.0	127.0	222.8	2.0	2.9	3.5	103.3	101.3	2.0	1.9
LGMTPM05 Seg03T18	16	230	9	113	230	10	17.0	229.3	111.8	230.8	1.3	1.5	3.7	104.8	106.4	1.6	1.5
LGMTPM05 Seg03T19	35	231	8	130	232	9	34.8	230.0	129.3	230.8	1.0	1.5	3.6	104.5	107.9	3.4	3.2
LGMTPM05 Seg03T20	37	220	9	130	224	10	37.5	221.3	132.3	222.3	1.3	2.9	3.9	104.8	106.8	2.0	1.9
LGMTPM05 Seg03T21	31	226	8	129	230	8	30.5	225.5	126.5	227.0	0.7	3.9	3.1	106.0	101.3	4.7	4.4
LGMTPM05 Seg03T22	47	220	9	144	223	10	48.8	219.3	145.3	220.3	1.9	3.0	4.0	106.5	105.9	0.6	0.6
LGMTPM04 Seg01T01	365	360	12	433	425	13	366.0	358.0	429.3	424.0	2.2	3.9	3.1	101.4	99.3	2.2	2.1
LGMTPM04 Seg01T02	366	362	13	430	427	14	365.8	362.5	429.0	429.5	0.6	2.7	3.2	102.1	104.0	1.8	1.8
LGMTPM04 Seg01T03	365	370	12	428	436	12	368.0	371.0	431.3	438.0	3.2	3.8	3.2	102.1	104.7	2.5	2.5
LGMTPM04 Seg01T04	367	378	11	429	449	11	367.3	379.3	431.5	445.3	1.3	4.5	4.0	102.1	101.2	0.9	0.9
LGMTPM04 Seg01T05	365	381	12	435	448	13	367.8	383.3	431.3	450.5	3.6	4.5	4.2	103.5	100.9	2.6	2.5
LGMTPM04 Seg01T06	363	375	14	429	453	15	368.3	380.0	433.0	450.0	7.3	5.0	3.6	105.4	102.3	3.0	2.9
LGMTPM04 Seg01T07	369	385	11	433	450	12	369.3	385.5	430.8	450.3	0.6	2.3	3.4	99.3	98.5	0.8	0.8
LGMTPM04 Seg01T08	370	381	11	432	455	11	370.3	385.3	432.8	451.1	4.3	4.0	3.1	100.7	103.7	3.0	3.0
LGMTPM04 Seg01T09	371	388	10	431	452	10	371.0	389.0	433.0	450.0	1.0	2.8	3.9	98.9	96.2	2.6	2.7
LGMTPM04 Seg01T10	373	389	9	433	450	9	375.0	389.3	430.3	451.0	2.0	2.9	3.2	92.8	95.0	2.2	2.4
LGMTPM04 Seg01T11	378	389	11	433	451	9	376.3	389.3	430.3	452.3	1.8	3.1	3.6	93.0	90.0	3.0	3.2
LGMTPM04 Seg01T12	375	389	9	432	455	9	377.8	389.0	430.3	451.0	2.8	4.4	4.9	91.2	96.1	4.9	5.3
LGMTPM04 Seg01T13	366	389	8	443	460	9	370.3	391.3	440.8	458.3	4.9	2.9	4.6	107.1	103.2	3.9	3.6
LGMTPM04 Seg01T14	370	390	10	439	454	10	372.5	392.3	438.5	451.0	3.4	3.0	4.8	98.3	96.1	2.2	2.2
LGMTPM04 Seg01T15	373	386	9	438	453	9	374.3	387.5	436.0	451.0	2.0	2.8	3.2	98.6	101.0	2.4	2.5
LGMTPM04 Seg01T16	372	391	9	430	452	11	375.3	389.5	430.3	451.0	3.7	1.0	3.3	92.5	93.9	1.4	1.5
LGMTPM04 Seg01T17	373	394	9	436	452	9	375.0	392.3	435.0	451.0	2.7	1.4	3.2	94.0	95.2	1.3	1.4
LGMTPM04 Seg01T18	378	389	9	435	450	9	375.3	386.0	430.3	451.0	4.1	4.9	3.5	95.2	92.0	3.1	3.3
LGMTPM04 Seg01T19	379	389	9	437	455	9	377.5	385.8	435.3	451.0	3.6	4.4	3.7	95.1	98.1	3.0	3.1
LGMTPM04 Seg01T20	378	389	9	438	453	9	377.9	388.0	436.3	451.0	1.0	2.7	3.9	95.9	96.1	0.2	0.2
LGMTPM04 Seg01T21	377	389	9	434	452	9	374.3	389.0	431.0	451.0	2.7	3.2	4.1	94.0	92.2	1.8	1.9
LGMTPM04 Seg01T22	370	387	9	439	448	9	369.3	386.0	440.3	451.0	1.3	3.3	5.1	106.3	102.0	4.3	4.0
LGMTPM04 Seg01T23	376	389	9	433	449	9	375.1	388.3	430.3	451.0	1.2	3.4	3.2	93.3	92.6	0.7	0.8
LGMTPM04 Seg01T24	372	389	9	433	449	9	375.3	389.3	430.3	451.0	3.3	3.4	4.0	92.6	92.7	0.1	0.1
LGMTPM03 Seg01T01	210	371	8	243	417	10	212.5	369.7	243.0	419.5	2.8	2.5	4.2	72.4	73.3	0.8	1.2
LGMTPM03 Seg01T02	215	372	9	245	419	11	213.3	370.0	246.5	421.5	2.6	2.9	3.9	71.3	73.6	2.3	3.2
LGMTPM03 Seg01T03	216	375	9	249	420	10	214.5	371.3	248.0	422.8	4.0	2.9	3.6	71.3	70.0	1.3	1.9